RSC Applied Interfaces

ROYAL SOCIETY OF CHEMISTRY

PAPER

View Article Online
View Journal | View Issue

Cite this: *RSC Appl. Interfaces*, 2025, **2**, 780

B,N co-doped V_2C nanoparticle embedded FeP nanoflake substrates as unique bifunctional electrocatalysts for overall water splitting in alkaline media†

Dasari Sai Hemanth Kumar, ‡[a] Manzoor Ahmad Pandit,‡[ab] Vinay Kumar Kolakaluri[a] and Krishnamurthi Muralidharan *[a]

Hydrogen energy as a solution to meet energy demands has highlighted the need for efficient and cost-effective electrocatalysts for hydrogen production through water electrolysis. Heterointerface materials with self-support have shown promising electrochemical performances due to their modulated electron structure, improved electrochemical surface area, and more active sites. In our study, we successfully synthesized a heterostructure material comprising iron phosphide (FeP) nanoflakes as a substrate, embedded with boron (B) and nitrogen (N) co-doped vanadium carbide (V_2C) nanoparticles through a hydrothermal method followed by pyrolysis. We prepared FeP@B,N-V_2C heterostructures to enhance efficiency using different weight ratios (5%, 10%, 15%, and 20%) of FeP substrates while adjusting B,N-V_2C nanoparticles accordingly. The catalytic applicability of these materials was evaluated in electrochemical water splitting in an alkaline medium. Compared to other heterostructures, 10% FeP@B,N-V_2C exhibited the highest catalytic activity, with overpotentials for the OER and HER in an alkaline medium of 260 mV and 235 mV, respectively, at a current density of 10 mA cm^{-2}. The low Tafel values were determined as 56.85 mV dec^{-1} and 118 mV dec^{-1}, with remarkable stability over 24 hours with a higher efficiency of 97.3%. The effectiveness and stability of electrocatalysts were corroborated by its ability in the overall water splitting (OWS), which occurred at a lower onset potential of 1.57 V@10 mA cm^{-2}. The low overpotentials and Tafel values observed in these catalysts are attributed to the heterojunction formed between the FeP nanoflakes and B,N co-doped V_2C nanoparticles. The enhancement in electrochemical activity resulting from the heterojunction is due to the higher surface area, increased porosity, decreased electrochemical resistance and the introduction in electroactive centres due to B,N co-doping. Consequently, this study provides a promising platform for developing novel nanomaterials for energy conversion applications.

Received 25th November 2024,
Accepted 7th March 2025

DOI: 10.1039/d4lf00394b

rsc.li/RSCApplInter

1. Introduction

The global energy crisis and environmental pollution highlight the need for alternative resources, such as hydrogen (H_2) produced through electrochemical water-splitting reactions.[1,2] This water-splitting process involves two half-cell reactions: the hydrogen evolution reaction (HER) at the cathode, which is a two-electron process, and the oxygen evolution reaction (OER) at the anode, which is a four-electron process. However, the slow kinetics and multi-electron transfer process involved in the HER and OER present significant challenges.[2–7] While noble metal catalysts like IrO_2 and RuO_2 have demonstrated exceptional electrochemical performances for the OER, Pt/C catalysts have shown superior catalytic activity for the HER. However, their high cost and limited availability restrict their widespread industrial application.[8,9] Therefore, there is a pressing need to develop efficient and cost-effective electrocatalysts to replace noble metal catalysts.

Research on electrocatalytic water splitting has shown promising developments in transition metal-based catalysts, including chalcogenides, phosphides, carbides, and nitrides. These materials have the potential to serve as cost-effective and stable alternatives due to their natural abundance, electrical conductivity, and optimal Gibbs free energy.[10–13] However, their practical application is limited by the weak binding strength between active sites and intermediates. To

[a] *School of Chemistry, University of Hyderabad, Hyderabad 500046, Telangana, India. E-mail: murali@uohyd.ac.in*
[b] *Materials Genome Institute, Shanghai University, Shanghai 200444, China*
† Electronic supplementary information (ESI) available. See DOI: https://doi.org/10.1039/d4lf00394b
‡ Both the authors contributed equally.

address this challenge, significant research efforts are focused on developing materials to overcome these binding issues. Among the catalysts, transition metal phosphides (TMPs) have received tremendous attention and proven to be the most promising catalysts.[14] It is revealed that the P atom in TMPs has better electronegativity to attract electrons from the transition metal atoms effortlessly, which enhances its electrical conductance.[15] Recently, several TMPs including Ni, Co and Fe phosphides have been used as HER or OER electrocatalysts in acidic or basic media with excellent performances.[16,17] The presence of d-orbitals makes TMPs act either as nucleophiles or electrophiles in chemical reactions, facilitating intermediate formation and reducing the active hydration energy barrier.[18–20] For example, based on DFT studies, Yao *et al.* found that the synergistic effect of 3d orbitals leads to high HER and OER activity.[21]

Among the TMPs, FeP garnered special attraction, because the Fe–P bond is found to stimulate the O_2 molecule, facilitating the HER/OER kinetics.[22–24] The HER mechanism on FeP catalysts resembles the catalytic reaction of [FeFe] hydrogenase enzymes.[25] Also, FeP catalysts can be moderately oxidized at certain potentials, leading to oxide and phosphate formation which further accelerate the OER kinetics.[26] The core–shell structures are found to reveal higher activity because of the high specific surface area, maximum active sites available and reduced charge transfer distances.[27,28] However, FeP activity is limited due to corrosion in both acidic and basic media. On the other hand, the activity of catalysts mostly depends on the structure as well as morphology.[29] In some cases, the self-supported FeP can act as a template due to its nanoflake structure, providing parallel elements that react with the other materials to form hierarchical structures.[30,31] However, earlier reports have revealed that phosphides with lone transition elements like FeP, Co_2P, NiP, *etc.*, have restricted electrochemical abilities.[32] Therefore, it's interesting to investigate composites, bimetals or alloys of TMPs for improved performances.

Transition metal carbides (TMCs) revealed excellent electrochemical performance and greater stability in the HER/OER comparable to Pt. Some reports stated that among TMCs, tungsten and molybdenum carbides are outstanding noble metal free electrocatalysts for water splitting.[33] However, in the case of VB group TMCs, vanadium based carbides were studied less in electrochemical activities.[34] It is found that vanadium carbide (VC) is abundantly available in the earth, making it a strong candidate for electrochemical activities.[35] But still, the electrochemical abilities of VC are underexplored and inadequate because of inappropriate interactions between the various reactive intermediates and the surface.[36,37] Therefore, the most effective way to enhance the electrocatalytic performance of VC is to dope it with foreign elements, and some recent reports describe this approach as a feasible way.[38] For example, Zhao *et al.*, reported the electrochemical OER performance of Pt-doped VC on the basis of DFT studies. The electrochemical performance indicated that the O* did not desorb from the surface easily because of the great Gibbs free energy, which requires an overpotential of 1.86 V. The Gibbs free energy barrier associated with the potential determining step in Pt-doped VC reduces the OER overpotential to 0.58 V, which comes close to 0.56 V of IrO_2. This indicates that the doping not only enhances the interactions between hydrogen and the VC surface, but also normalises the interaction of intermediates during the OER.[39]

Besides doping, structural transformation is another way to enhance the number of active sites including the formation of porous structures, quantum dots, nanosheets/flakes, *etc.*, thereby modifying the electrochemical ability of catalysts.[34] For example, Peng *et al.* claimed that the graphitized carbon engrained in the VC/nickel heterostructure exhibits excellent results in electrochemical HER activity due to the synergetic effect between the various constituents of the heterostructure.[38] Likewise, Mengmeng Shao *et al.* synthesized N-doped VC, which showed high water splitting performance compared to pure VC.[40] Based on the above discussion, the co-doping of B and N in V_2C embedded FeP nanoflakes is projected to substantially enhance the electrochemical water splitting. Further, to prevent the aggregation of nanoparticles and improve the electrochemical activity as well as stability under harsh conditions, the nitrogen doped carbon was synthesized as a substrate, which reduces the corrosion rates.[41] Various reports claimed that addition of B and N on carbon substrates revealed enhanced catalytic results rather than the either pure N or B-doped catalysts.[42] However, the low doping concentrations of B and N may lead to the formation of electrochemically inactive B–N bonds, which can hinder the catalytic abilities of these B–N co-doped electrocatalysts.[43,44] In particular, the addition of either B or N improves the electrical conductance of carbon based materials by reducing the energy gap, and increasing the density of states at finite and zero energy. For instance, Joshi *et al.* demonstrated the synthesis of B and N co-doped r-GO containing B–N, B–C, and N–C functional groups, which enhance the stability of IrO_2 nanoparticles and elevate the electrochemical water splitting efficiency.[45] However, the barriers couldn't be completely removed due to the complex nature of the system. Therefore, it is vital to develop a controlled strategy for dual doping to construct an effective system while maintaining a robust structure–activity relationship.

In our study, we highlight a heterojunction material, FeP@B,N-V_2C, which was produced by depositing B,N co-doped V_2C nanoparticles onto FeP nanoflakes acting as a substrate using a hydrothermal method with subsequent pyrolysis. We examined with different weight ratios of FeP and B,N-V_2C, to achieve a controllable and effective electrocatalytic activity. The resulting electrocatalysts exhibited promising electrochemical activity in water splitting for both the HER and OER. Notably, 10% FeP@B,N-V_2C demonstrated the best catalytic activity among the various heterostructures, with overpotentials of 260 mV and 235 mV

at a current density of 10 mA cm^{-2} for the OER and HER, respectively, in an alkaline medium. Additionally, this particular composition displayed remarkable durability over 24 hours for both the OER and HER. Encouraged by this excellent bifunctional performance, we further evaluated the overall water-splitting reaction of 10% FeP@B,N-V_2C using a two-electrode cell, which demonstrated outstanding electrochemical performance and remarkable durability. Consequently, our work establishes that the heterojunction formed between FeP and B,N-V_2C exhibits promising performance for water splitting (OER/HER) reactions, suggesting a new avenue for the development of materials for green energy generation.

2. Experimental section

2.1. Materials

Ammonium metavanadate (NH_4VO_3), ferrous sulphate dihydrate ($FeSO_4{\cdot}2H_2O$), sodium hypophosphite monohydrate ($NaH_2PO_2{\cdot}2H_2O$), melamine, glucose, boric acid, ammonia, potassium hydroxide, hydrogen peroxide, and Nafion were purchased from Sigma Aldrich. Millipore water was used for the electrochemical reactions. All listed chemicals were of analytical grade and used without further processes.

2.2. Instrumentation

The synthesized FeP@B,N-V_2C materials were characterized by various techniques for their structural, morphological, and elemental information. The powder X-ray diffraction (PXRD) structure and phase were interpreted by employing a Bruker D8 Advance spectrometer (CuKα, λ = 1.54056° A, 2θ = 20° to 70°). Field Emission Scanning Electron Microscopy (FESEM), Transmission Electron Microscopy (TEM), and Energy-Dispersive X-Ray Spectroscopy (EDS) techniques were utilized for determining the morphology and elemental analysis of the heterostructures by employing an Ultra 55 Carl Zeiss microscope with operating voltage = 10 kV and TEM (FEI Tecnai G^2 F20 STEM with 200 kV). The specific surface area and pore size distribution were studied by nitrogen adsorption–desorption isotherms with a Brunauer–Emmett–Teller instrument (BET) (Nova 2000e, Quantachrome Instruments Limited, USA, using liquid nitrogen (77 K)). X-ray photoelectron spectroscopy (XPS) (Thermo Scientific Escalab 250Xi spectrometer with Al-Kα radiation) was employed to determine the oxidation states and the chemical structure of the elements in the heterostructures. The electrochemical activities for performing the HER/OER of the different synthesized materials were studied by using a CHI6112E electrochemical workstation with a three-electrode arrangement.

2.3. Synthesis of FeP@B,N-V_2C heterostructures

(a) Synthesis of B,N-V_2C nanostructures. B,N-V_2C nanostructures were synthesized using a simple hydrothermal approach followed by pyrolysis. In this method, V_2C nanoparticles were synthesized first as follows: ammonium metavanadate (500 mg, 4.27 mmol), melamine (269 mg, 2.13 mmol) and glucose (770 mg, 4.27 mmol) were placed in 60 ml distilled water and stirred for one hour to make a homogeneous solution. It was then transferred into a Teflon container, which was placed in a stainless-steel autoclave and set at 180 °C for 12 h. After the reaction, the mixture was washed with methanol and acetone multiple times, dried at 70 °C overnight, and further set to pyrolysis at 450 °C for 2 h under a N_2 atmosphere to yield the pure V_2C nanostructure. For B and N dual doping, V_2C nanoparticles were dispersed in 60 ml distilled water along with a certain amount of boric acid followed by ammonia. It was placed in an autoclave and the reaction conditions were adjusted at 180 °C for 12 h. The synthesized product was washed with methanol and acetone several times and dried in an oven at 70 °C overnight to yield B,N co-doped V_2C nanoparticles.

(b) Synthesis of FeP nanoflakes. FeP was synthesized by stirring it at room temperature, followed by pyrolysis. In this method, $FeSO_4{\cdot}2H_2O$ (3.97 g) was placed in a round-bottomed flask containing 100 ml of distilled water, and 10 ml of 5 M KOH was added dropwise into the Fe precursor solution followed by the addition of 5 ml of 30% H_2O_2 to form a red colour precipitate solution. The precipitate was washed several times with distilled water until it neutralized to yield FeOOH nanoparticles. The as-synthesized FeOOH nanoparticles were then placed in a quartz tube along with excess amount of $NaH_2PO_2{\cdot}2H_2O$ and set to undergo pyrolysis at 300 °C for 2 h in an inert atmosphere to obtain FeP nanoflakes.

(c) Synthesis of the FeP@B,N-V_2C nanocomposite. The final desired FeP@B,N-V_2C nanocomposite was synthesized through a sonication method. In order to optimize the efficiency of the as-synthesized heterostructure FeP@B,N-V_2C, the different weight percentages (5%, 10%, 15%, and 20%) of FeP were added into a dispersed solution of B,N-V_2C nanoparticles and sonicated for 30 min. The final prepared nanomaterials were centrifuged, washed with acetone and dried at 70 °C for 2 h.

2.4. Preparation of working electrodes for the HER/OER

In order to evaluate the electrochemical water-splitting performance of the synthesized materials (FeP@B,N-V_2C), a three-electrode cell was established. The working electrode consisted of the synthesized materials coated on nickel foam (NF, 0.5 cm × 2 cm), while a saturated calomel electrode served as the reference electrode and a graphite rod acted as the counter electrode. These electrodes were immersed in a 1 M KOH alkaline medium. The electrocatalysts were coated on the NF by forming a slurry of 2 mg of catalyst, 400 μL ethanol, 500 μL Millipore water, and 30 μL Nafion. The coatings were applied three times and then dried overnight in an oven. The electrochemical activity was obtained multiple times to ensure the reliability of the results. The potentials were calibrated with reference to the reversible hydrogen electrode (RHE) using the

equation $E_{RHE} = E_{SCE} + 0.241 + 0.0591$ pH. The onset overpotential (@j_{10} mA cm^{-2}) and Tafel plots (log(j) *versus* potentials (RHE)) were determined by performing Linear Sweep Voltammetry (LSV) at a scan rate of 5 mV s^{-1}. The double-layer capacitance (C_{dl}) was calculated from cyclic voltammetry (CV) measurements at sweep rates ranging from 20 mV s^{-1} to 200 mV s^{-1}. Electrochemical Impedance Spectroscopy (EIS) was also conducted at a frequency range of 100 kHz to 100 mHz with an amplitude of 10 mV.

3. Results and discussion

3.1. Synthesis and characterization

We successfully synthesized the desired materials, FeP@B and N-V_2C, using a straightforward hydrothermal approach (Scheme 1) without adding any external capping agent or stabilizer. The synthesis involved boron and nitrogen co-doped V_2C nanoparticles dispersed on FeP nanoflakes. Initially, V_2C nanoparticles were prepared using the hydrothermal approach with glucose and melamine as carbon sources and morphology directional agents. Boron and nitrogen were doped onto the V_2C nanostructures to improve their electrochemical performance. Next, iron oxyhydroxide was prepared by slightly modifying a reported method, which involves rapidly oxidizing precipitated Fe^{2+} salt.[46,47] This intermediate was then subjected to pyrolysis with a phosphorus source under a constant nitrogen flow to yield FeP nanoflakes. Composites of optimized activity were synthesized using different weight ratios (5%, 10%, 15%, and 20%) of FeP and B,N-V_2C through ultrasonication. Ultrasonication is a consistent method to redisperse nanopowders in liquids and the insertion of nanomaterials into mesoporous materials without changing the intrinsic physicochemical properties of the base materials.[48,49]

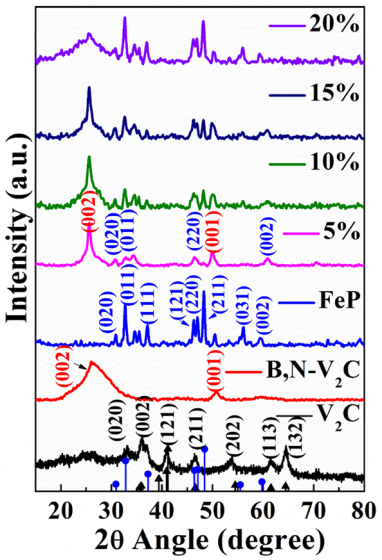

Fig. 1 The PXRD patterns of pure V_2C, B,N-V_2C, pure FeP, and the composite FeP@B,N-V_2C nanomaterials (5%, 10%, 15%, 20% ratios).

The synthesized nanostructures, FeP@B,N-V_2C, were initially characterized using PXRD to determine the phase purity of the materials. The PXRD pattern (Fig. 1) revealed that V_2C nanoparticles exhibited a crystalline XRD pattern with prominent diffraction peaks at 2θ values of 33.12°, 35.95°, 41.07°, 46.59°, 53.71°, 61.46° and 64.51°, corresponding to the (020), (002), (121), (211), (202), (113) and (132) planes, consistent with the orthorhombic phase of V_2C (JCPDS no. 71-1272). However, upon boron and nitrogen

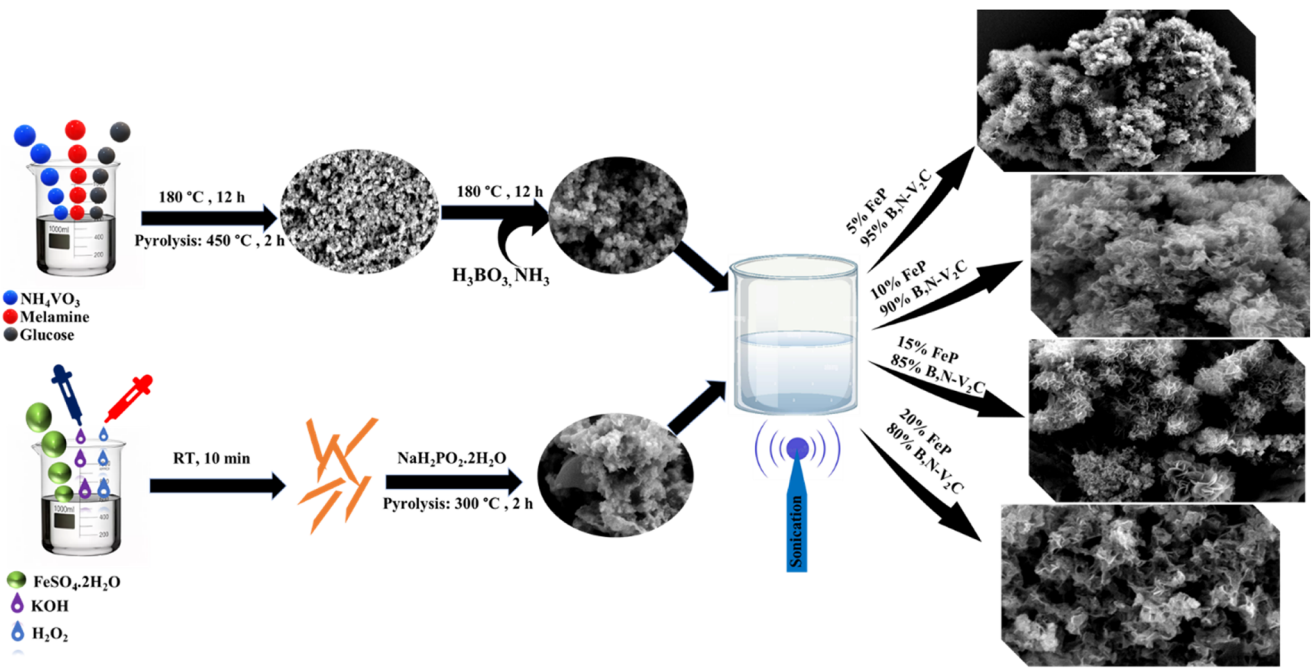

Scheme 1 Illustration for the synthesis of FeP@B,N-V_2C heterostructures.

doping, most of the V_2C peaks were obscured, reducing the crystallinity of the V_2C nanostructures. Two new peaks emerged, one broad peak at around 2θ of 25° and another less intense peak at 50°, corresponding to the (002) and (001) planes, confirming the boron and nitrogen doping.[50,51] Similarly, pure FeP nanoflakes exhibited intense XRD patterns at 2θ values of 30.81°, 32.73°, 34.52°, 35.41°, 37.08°, 46.27°, 46.97°, 48.31°, 50.35°, 56.05°, and 59.39°, with the corresponding lattice planes of (020), (011), (200), (120), (111), (121), (220), (211), (130), (031), and (002), indicating the orthorhombic phase of pure FeP (JCPDS no. 89-4863).[52] Upon increasing the percentage (5%, 10%, 15%, and 20%) of FeP, the XRD pattern revealed that all the peaks of B,N-V_2C were related to the orthorhombic phase of FeP nanoflakes. The intensity of the peaks around 2θ of 25° and 50° increased with the rise in FeP percentage, indicating the formation of composite nanomaterials, as depicted in Fig. 1. Also, in the composites, it is observed that the peaks around 2θ of 33°, 34° and 46° were merged with their intensity further increasing as the FeP amount is increased, while the peak around 60° slightly shifted towards a higher 2θ value. This further confirmed the heterostructure formation between the B,N co-doped V_2C nanoparticles and FeP nanoflakes.

The XPS data were acquired to provide a comprehensive understanding of the structure of the synthesized nanocomposites, encompassing their elemental composition and valence states. To confirm the electronic interaction in the composite formation, we have performed XPS analysis of individual FeP and B,N-V_2C nanoparticles as shown in Fig. S4.† The survey spectra (Fig. S3a and S4a and b†) of the 10 wt% FeP@B,N-V_2C nanostructures and FeP, B,N-V_2C nanoparticles validate the presence of all anticipated elements, namely Fe, P, B, N, V, and C in the material. In the XPS spectrum of V 2p (Fig. 2c), two peaks were further split into two peaks at binding energies of 515.95 eV, 517.2 eV, 523.05 eV, and 524.53 eV attributed to V^{3+} $2p_{3/2}$, V^{4+} $2p_{3/2}$, V^{3+} $2p_{1/2}$, and V^{4+} $2p_{1/2}$, respectively. In the case of V 2p of V_2C (Fig. S4g†), two peaks ($2p_{3/2}$ and $2p_{1/2}$) are deconvoluted into two peaks with binding energies of 515.71 eV, 517.09 eV, 522.89 eV, and 524.60 eV attributed to V^{3+} $2p_{3/2}$, V^{4+} $2p_{3/2}$, V^{3+} $2p_{1/2}$, and V^{4+} $2p_{1/2}$, respectively. Regarding the C 1s spectrum (Fig. 2d), the binding energies of 283.84 eV, 284.65 eV, 286.09 eV, and 288.05 eV are associated with V–C, C–C, C–O, and O–C=O bonds, respectively.[53–55] For the deconvolution of C 1s (Fig. S4h†), binding energies of 284.67 eV, 285.44 eV, and 287.69 eV are attributed to C–C, C–O, and O–C=O bonds, respectively. The confirmation of boron and nitrogen doping onto V_2C nanoparticles can be ascertained from the XPS spectra of boron (B 1s) and nitrogen (N 1s), as depicted in Fig. 2(a) and (b). In the B 1s XPS spectrum, B–C sp^2, B–N peaks were observed, indicating the connection of boron atoms to carbon atoms of V_2C nanoparticles. In the N 1s XPS spectrum, binding energies of 398.5 eV, 399.9 eV, and 400.5 eV correspond to C=N, C–N, and B=N–C bonds, respectively, denoting the interaction of carbon of V_2C nanoparticles with nitrogen.[56–58] Similarly, doping of B and N onto V_2C nanoparticles were confirmed by the B 1s and N 1s XPS spectra (Fig. S4e and f†), with binding energies of 192.3 eV, 398.67 eV, 400.08 eV, and 400.78 eV attributed to B–C, N=C, N–C, and B=N–C respectively. The Fe 2p XPS spectra (Fig. 2e) exhibit binding energies of 711.4 eV and 724.4 eV, indicating the presence of Fe^{3+} $2p_{3/2}$ and Fe^{3+} $2p_{1/2}$, with the energies at 714.05 eV and 726.44 eV attributed to the satellite peaks of Fe^{2+}. Likewise, the Fe 2p spectra (Fig. S4c†) deconvoluted into two peaks with

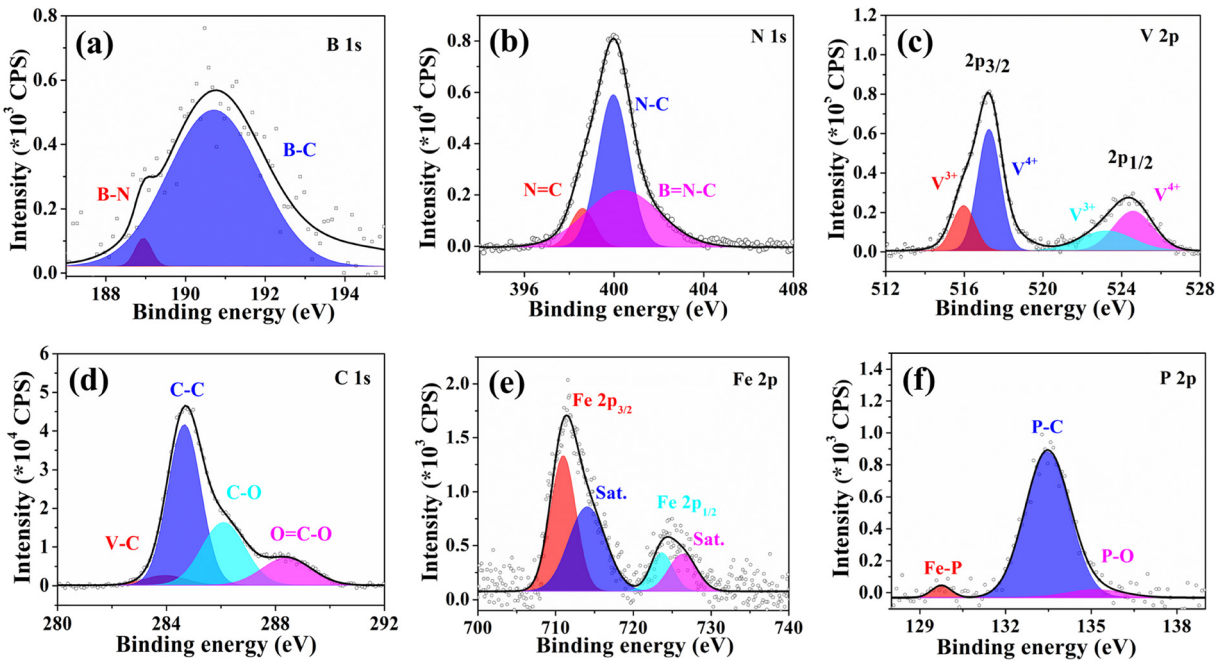

Fig. 2 XPS binding energies of (a) B 1s, (b) N 1s, (c) V 2p, (d) C 1s, (e) Fe 2p, and (f) P 2p of 10% FeP@B,N-V_2C, respectively.

binding energies of 712.74 eV and 726.26 eV attributed to Fe^{3+} $2p_{3/2}$ and Fe^{3+} $2p_{1/2}$, with satellite peaks of 716.21 eV and 729.83 eV, confirming the presence of Fe^{2+}, and a small peak at the binding energy 707.61 eV attributed to Fe–O bonds, indicating the slight oxidation during pyrolysis. Similarly, the P 2p XPS spectra (Fig. 2f) display three peaks at 129.7 eV, 133.5 eV and 135.1 eV, related to the Fe–P, P–C and P–O bonds, respectively. In the case of P 2p XPS spectra (Fig. S4d†), it is deconvoluted into two peaks with binding energies of 130.37 eV and 134.50 eV attributed to Fe–P and P–O bonds, as corroborated by the previous literature.[59–69] Consequently, the aforementioned XPS data provides compelling evidence regarding the formation of the composite materials, further affirming and substantiating the successful deposition of V_2C nanoparticles on the FeP nanoflakes. There is a slight shift in binding energies with the heterostructure compared to individual nanoparticles, which is an evident proof that the composite materials are not just a physical mixture and there is coupling linkage between FeP and B,N-V_2C during the synthesis of the heterostructure.

Based on the UV-vis absorption spectrum analysis, it was observed that the composite nanostructures and pure materials (Fig. S3b and c†) exhibited broad absorption in the UV-vis and NIR regions, respectively. The bandgap values, ranging from 0.98 eV to 1.25 eV for the synthesized nanostructures, were determined using the Tauc plot (eqn (1)).[67]

$$\alpha h\gamma = A(h\gamma - E_g) \quad (1)$$

3.2. Morphology and surface area

The morphology of the as-synthesized nanocomposites, including B,N-V_2C, pure FeP, and FeP@B,N-V2C, was analyzed using FESEM (Fig. 2). In Fig. 3a, the undoped V_2C exhibits a spherical morphology with a highly crystalline nature. Upon doping V_2C with boron and nitrogen, the spherical morphology is retained but with a larger average particle size. The overall crystallinity is reduced, and the material appears slightly amorphous, as observed in PXRD (Fig. 3b). The pure FeP displays a flower-type morphology with protruding petals growing outwards vertically along the (211) direction as shown in Fig. 3c.

The composite structures present a significantly different image compared to pure FeP and B,N co-doped V_2C. A combination of well-dispersed particles and fully developed flowers is clearly visible. At a 5% weight ratio, the FeP@B,N-V2C heterostructure exhibits flower growth, confirming the dispersion of B,N co-doped V_2C nanoparticles onto FeP nanoflakes, resulting in enlarged petals as depicted in Fig. 3d. As the weight ratio of FeP increases, the B,N-V_2C nanoparticles are uniformly distributed onto the nanoflakes, resulting in compact and dense flowers, as shown in Fig. 3e. Notably, at a 15% weight ratio, fully grown and well-developed flowers with thin petals are abundantly found, as displayed in Fig. 3f. However, the increase in weight percentage does not follow a consistent trend. For the 20% weight ratio, thick and short flowers were observed.

The elemental distribution of pure FeP, pure V_2C, B,N co-doped V_2C, and FeP@B,N-V_2C nanocomposites was determined using EDS and elemental mapping images. These analyses revealed the presence of added elements during their synthesis, including Fe, P, V, C, B, and N within all nanostructures, in accordance with stoichiometric ratios (Fig. S1 and S2†).

The morphology of the synthesized materials was further analyzed using TEM, which exhibited good agreement with the images obtained from FESEM. The TEM images in Fig. 4a1 and b1 depict the spherical particle nature of pure V_2C with an average particle size of 18.03 nm (inset of Fig. 4a2), consistent with the observations from the FESEM images, and similar observations were made for the B,N co-doped V_2C with an average particle size of 25.02 nm (inset of

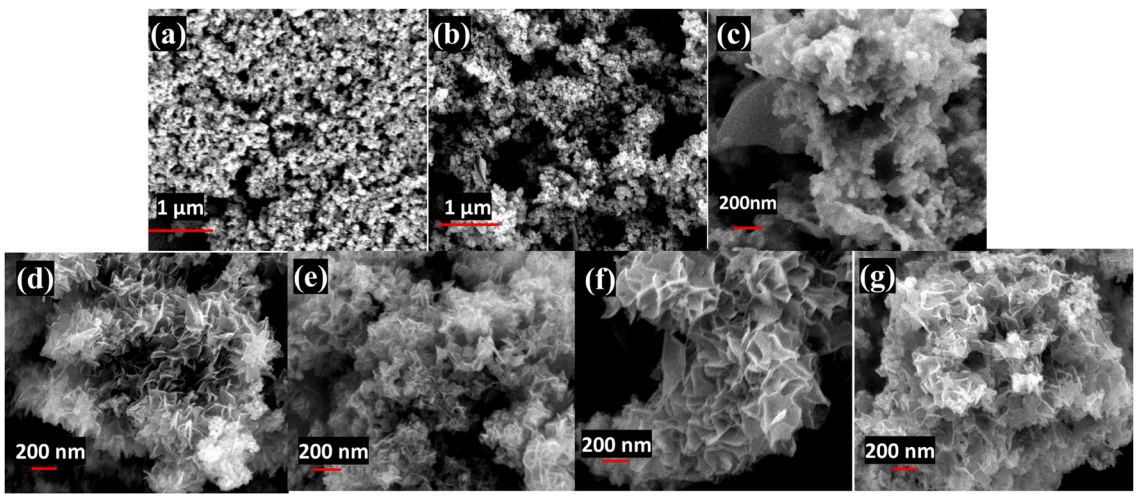

Fig. 3 The morphological analysis showing high magnification FESEM images of (a) pure V_2C, (b) B,N-V_2C, (c) FeP and (d) 5%, (e) 10%, (f) 15%, and (g) 20% wt. ratios of B,N-V_2C@FeP nanostructures.

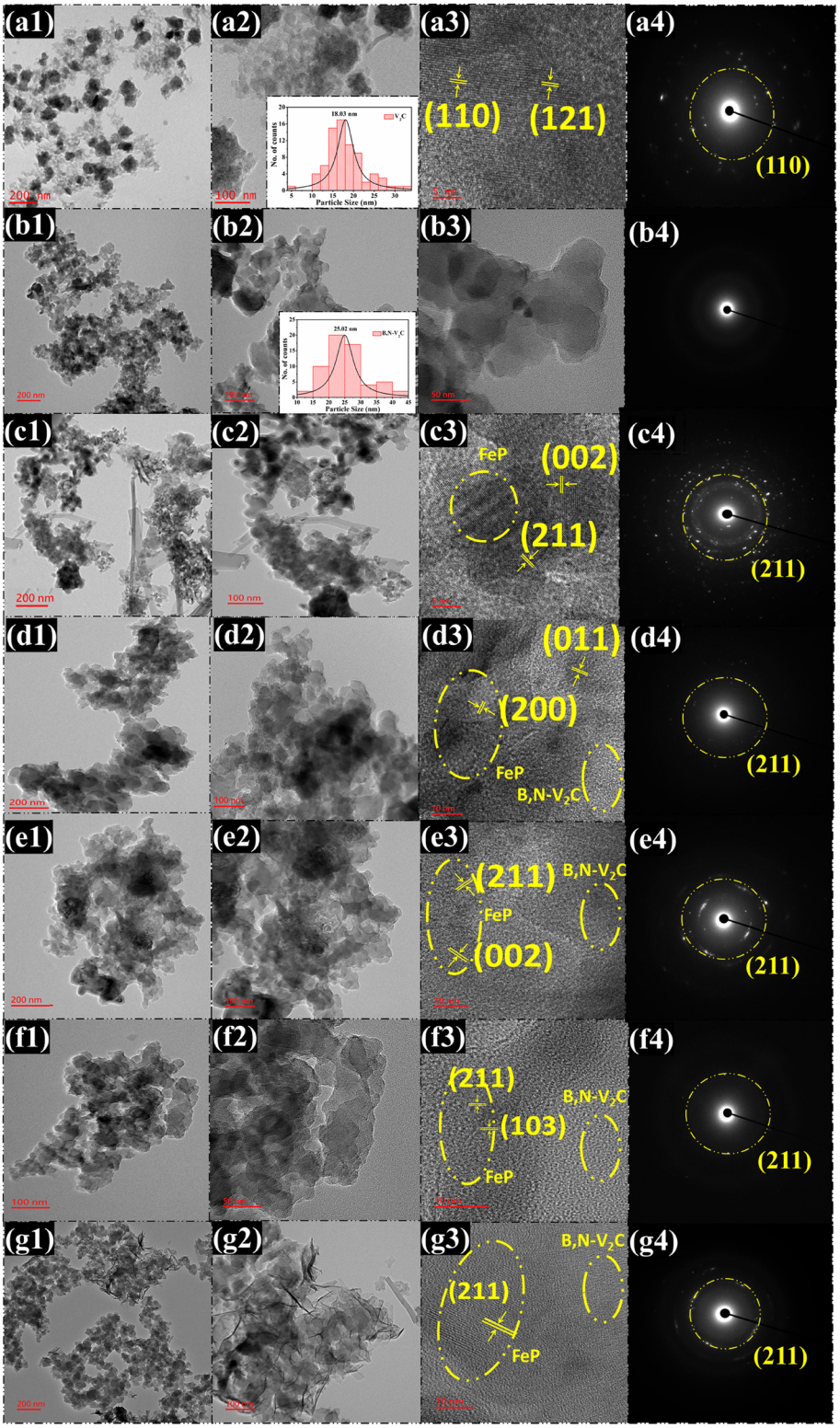

Fig. 4 The morphological analysis showing TEM, HRTEM and SAED pattern images of (a1–a4) pure V_2C (inset: particle size histogram), (b1–b4) B, N-V_2C (inset: particle size histogram), and (c1–c4) FeP and (d1–d4) 5%, (e1–e4) 10%, (f1–f4) 15%, and (g1–g4) 20% wt. ratios of FeP@B,N-V_2C nanostructures.

Fig. 4b2). High-resolution TEM (HRTEM) images (Fig. 4a3 and b3) of pure V_2C and B,N co-doped V_2C nanoparticles revealed that the lattice planes could be indexed to the (110) and (121) planes, with corresponding *d*-spacings of 3.57 and 2.18 nm, which is in good agreement with PXRD results. The selected area electron diffraction

(SAED) patterns (Fig. 4a4 and b4) displayed bright spots corresponding to the (110) and (121) planes, confirming the crystalline nature of V_2C nanoparticles. In contrast, no bright spots were visible in the doped V_2C, indicating the amorphous nature of the B,N co-doped V_2C nanoparticles.

The nanostructure of FeP, as depicted in Fig. 4c1, exhibits a flower-like morphology with vertically grown flakes. The corresponding *d*-spacing values of 2.95 and 1.91 nm (Fig. 4c3) can be associated with the (002) and (211) planes, showing good agreement with the PXRD pattern. The SAED patterns (Fig. 4c4) display distinct bright rings of the (211) planes, indicating the high crystallinity of FeP nanoflakes. Additionally, the TEM images of the composite materials with weight ratios of 5%, 10%, 15%, and 20% were examined alongside their pure material counterparts. Fig. 4d1 illustrates the TEM image of the 5% heterostructure, revealing the homogeneous dispersion of B,N co-doped V_2C nanoparticles on FeP nanoflakes. The deposition of nanoparticles on FeP nanoflakes and their role as the substrate are evident in the encircled regions in the figure. The corresponding HRTEM image and SAED patterns (Fig. 4d3 and d4) align well with the individual nanostructures. Similar TEM morphological observations were noted for the other composite materials (10%, 15%, and 20% weight ratios). It was observed that with an increase in FeP weight ratio, the B,N co-doped V_2C nanoparticles were well dispersed onto the nanoflakes, consistent with the FESEM images. The morphological studies conducted using FESEM and TEM are concordant with each other and with the PXRD patterns of the synthesized materials.

The catalytic activity of materials heavily depends on the specific surface area, making it a critical parameter. The surface analysis of the synthesized materials was conducted through N_2 adsorption–desorption analysis and BET isotherms. Fig. 5a–d illustrate the adsorption isotherms of B,N co-doped V_2C nanostructures with varying weight ratios (5%, 10%, 15%, and 20%). These curves exhibit a type IV isotherm, indicating the mesoporous nature of the composites. Among the different weight percentages synthesized, the 10% FeP@B, N-V2C nanostructure exhibits the highest surface area (146.08 $m^2\ g^{-1}$), followed by 5% (143.59 $m^2\ g^{-1}$), 15% (132.72 $m^2\ g^{-1}$), and 20% (111.28 $m^2\ g^{-1}$). Additionally, the pore size distribution corresponding to these weight percentage ratios is determined using the BJH method (Fig. S5a–d†), confirming the mesoporous nature of the composite materials. The larger surface area of the 10% FeP@B,N-V_2C nanostructure further elucidates its superior electrocatalytic behavior towards the HER and OER, indicating the presence of numerous active sites on the nanostructures.

3.3. Electrochemical oxygen evolution reaction (OER)

The synthesized materials were evaluated for their catalytic performance in electrochemical water splitting. A three-electrode system was employed to assess the electrochemical water splitting (HER/OER) capabilities of the synthesized nanostructures, including pure FeP, B,N-V_2C, and FeP@B,N-V_2C nanocomposites. The working electrode was created by depositing the synthesized material on nickel foam (NF) to provide active sites on the electrode, with saturated calomel as the reference electrode and a graphite rod as the counter electrode, in a 1 M KOH alkaline medium. Linear sweep voltammetry (LSV) measurements revealed that the overpotential obtained for 10% FeP@B,N-V_2C was lower at 260 mV compared to 5% (310 mV), 15% (298 mV), and 20% (297 mV) at 10 mA cm^{-2} current density for the OER. At the same current density, the pure FeP nanoflakes, V_2C

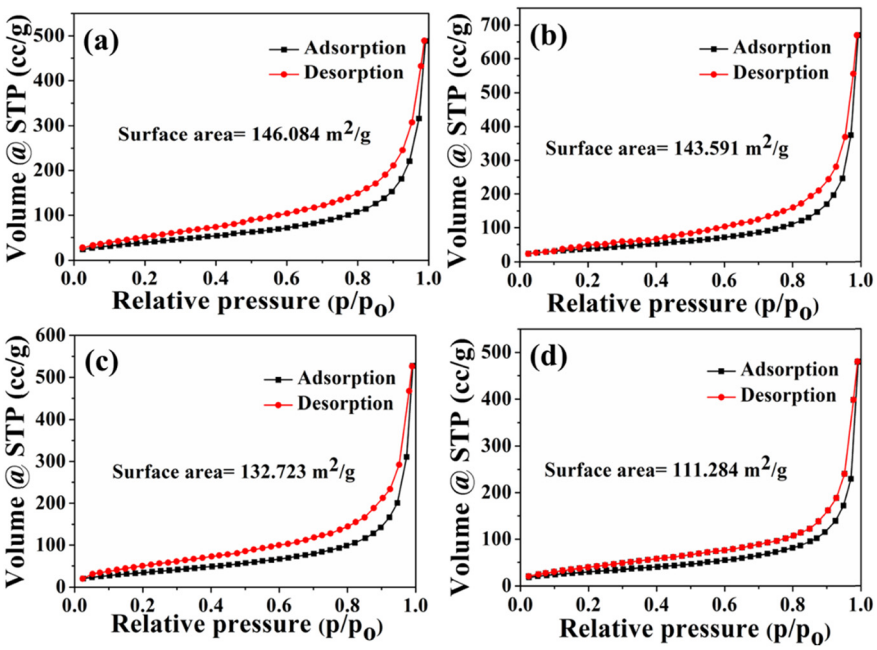

Fig. 5 (a–d) Nitrogen adsorption–desorption isotherms of 5%, 10%, 15%, and 20% wt. ratios of FeP@B,N-V_2C nanostructures, respectively.

nanoparticles, and B,N-V_2C nanoparticles exhibited significantly higher overpotentials of 290, 379, and 360 mV, respectively, while RuO_2 showed an overpotential of 312 mV. The presence of nitrogen constructively modifies the electronic structure and increases the active sites by modifying the charge distribution. Also, the introduction of heteroatoms like B and N simultaneously into carbon hybrids disrupts the charge-neutralities of carbon atoms and as a result, the heterostructure of B,N-doped V_2C with FeP nanoflakes produced significant results in the electrochemical oxygen reduction reaction.[70]

In order to further validate the effectiveness of OER catalysis, Tafel plots were generated (Fig. 6b). The Tafel plots were derived from the linear segment of the LSV (linear sweep voltammetry) curve, based on the Tafel equation ($\eta = a + b\log|j|$, where b represents the Tafel slope, η denotes the overpotential, and j indicates the current density). The plots indicated the following trend: the 10% weight ratio exhibited the lowest Tafel slope (56.85 mV dec^{-1}) when compared to the 5% (76.9 mV dec^{-1}), 15% (81.8 mV dec^{-1}), and 20% (74.2 mV dec^{-1}) weight ratios. The individual materials RuO_2, FeP, V_2C, and B,N-V_2C demonstrated Tafel slopes of 197, 74.3, 111.8, and 84.2 mV dec^{-1}, respectively, which correlated with the observed overpotential values for these materials. Notably, the 10% FeP@B,N-V_2C heterostructure exhibited the lowest overpotential and Tafel slope values, suggesting minimal interference with charge carriers and superior mass transport behavior, thus positioning it as a promising electrocatalyst.

The superior OER performance exhibited by the synthesized electrocatalysts may be attributed to the synergistic effect between the components, which enables better transfer of charge carriers and enhances catalytic activity. The charge transfer resistance (R_{ct}) values were determined through Electrochemical Impedance Spectroscopy (EIS) studies conducted in the frequency range of 100 kHz to 100 mHz, as illustrated in Fig. 6c. Analysis of the Nyquist plots revealed a smaller semicircle for 10% FeP@B,N-V_2C compared to the other composite materials,

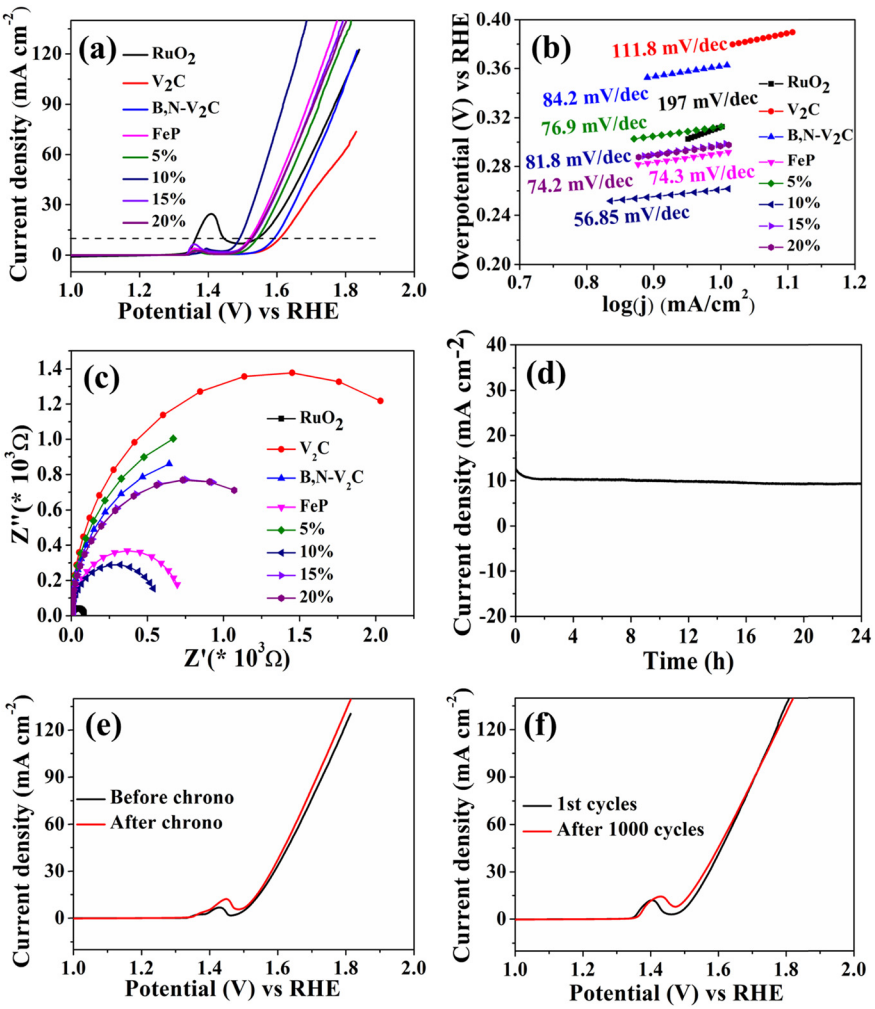

Fig. 6 (a) Polarisation curves for the OER. (b) Tafel plots and (c) EIS curves of FeP@B,N-V2C heterostructures and pure FeP and B,N-V_2C NPs. (d) Chronoamperometry (*i*–*t*) studies and comparison of polarisation curves (e) before and after chronoamperometry and (f) 1000 CV cycles of the 10% FeP@B,N-V_2C heterostructure.

indicating lower impedance to the transfer of charges, thereby facilitating rapid electron transfer from the substrate to the catalyst and promoting faster reaction kinetics (refer to Table S1 in the ESI†).

The stability and durability of the material are crucial factors for an electrocatalyst. The electrochemical durability of the electrocatalyst was confirmed by conducting both chronoamperometry (*i–t*) and continuous CV cycle studies, as depicted in Fig. 6d–f. The peak around 1.4 V is related to the onset of the OER on the working electrode nickel foam (NF). This observation indicates where the nickel-based catalysts begin to smoothen the OER, forming new active sites like NiOOH or $Ni(OH)_2$ phases. A stable OER performance was observed between 1.5 V and 1.8 V.[1,71] The study revealed that there was no significant change in the current density and overpotential after 24 hours of stability testing, indicating the long-term durability of the 10% FeP@B,N-V_2C electrocatalyst and other heterostructures for the OER (Fig. S6†). Similarly, there were insignificant changes in the overpotential after 1000 cycles of the 10% FeP@B,N-V_2C catalyst compared to other materials and pure components (Fig. S6†), demonstrating the excellent corrosion resistance of the catalyst. Therefore, the stability tests suggest a smooth transfer of charge carriers and efficient mass transfer across the electrolyte–electrode interface.

In order to delve deeper into the kinetics of the electrocatalysts, we measured the electrochemical double-layer capacitance (C_{dl}) and electrochemical surface area (ECSA) values by conducting CV cycles with scan rates ranging from 20 to 200 mV s^{-1} within the potential range of 1.14–1.26 V *vs.* RHE for 10% FeP@B,N-V_2C (Fig. 7a and b) and the remaining materials (Fig. S8†). We found that the ECSA value for 10% FeP@B,N-V_2C (1.96 mF cm^{-2}) was higher than those for the other heterostructures. This difference may be attributed to the distinctive distribution of double-doped V_2C nanoparticles, resulting in a maximum surface area and more active sites, which in turn enhances the C_{dl}/ECSA values (refer to Table S1 in the ESI†) and facilitates faster charge/ion diffusion within the electrolyte–electrode interface. The volumetric analysis of O_2 produced (Fig. S12a†) indicated a faradaic efficiency of 97.3% for 10% FeP@B,N-V_2C, with similar efficiencies of 96.4%, 95.8%, and 93.4% observed for the other heterostructures. The quantification of oxygen evolved using GC-TCD (as shown in Fig. S13a†) confirmed these results.

3.4. Electrochemical hydrogen evolution reaction (HER)

The dual functionality of the electrocatalyst was further investigated by testing its hydrogen evolution reaction (HER) activity, which yielded results comparable to its OER activity. The polarization curves for the Linear Sweep Voltammetry (LSV) measurements are illustrated in Fig. 8a, revealing an overpotential of 235 mV at a current density of 10 mA cm^{-2} for the 10% FeP@B,N-V_2C catalyst. Similarly, overpotentials of 258 mV, 263 mV, and 271 mV at the same current density were observed for the 5%, 15%, and 20% FeP@B,N-V_2C catalysts, respectively. In comparison, the overpotentials were 92 mV, 260 mV, 271 mV, and 258 mV for Pt/C, pure FeP, V_2C, and B,N-V_2C, respectively. Similar to the OER, the electrocatalysts also exhibited superior performance in the HER.

In order to gain a deeper understanding of the kinetics of the HER, Tafel plots were obtained (Fig. 8b). The Tafel slope

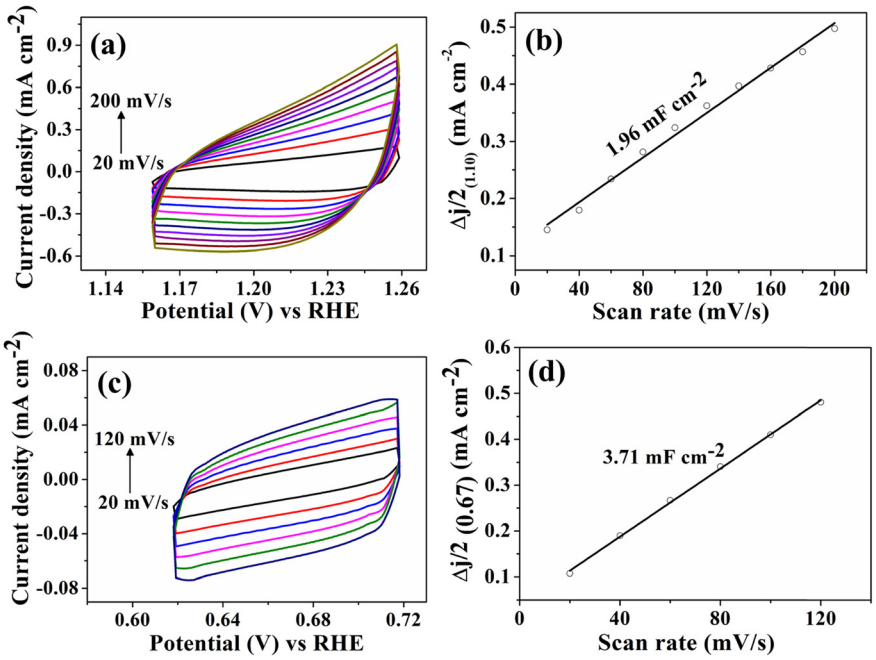

Fig. 7 Cyclic voltammograms and linear fit plots for (a and c) the OER and (b and d) HER at different scan rates from 20 mV s^{-1} to 200 mV s^{-1} of the 10% FeP@B,N-V_2C nanostructure, respectively.

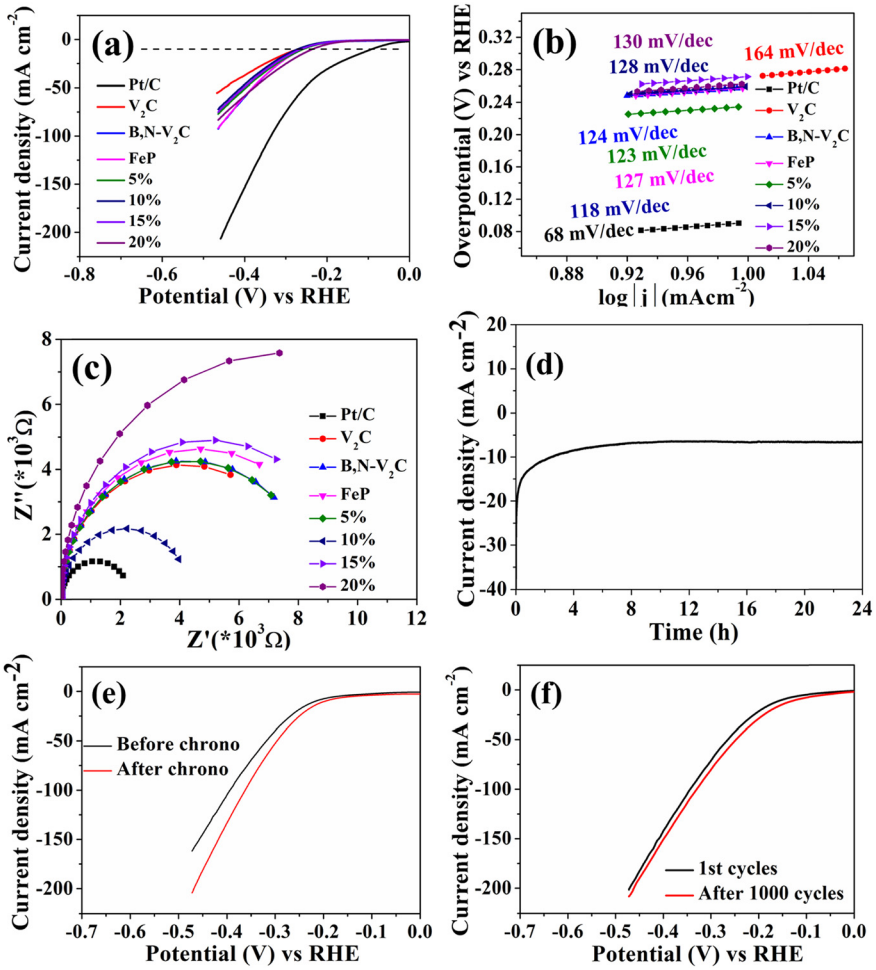

Fig. 8 (a) Polarisation curves for the HER. (b) Tafel plots and (c) EIS curves of FeP@B,N-V_2C heterostructures and pure FeP and B,N-V_2C NPs. (d) Chronoamperometry (*i*–*t*) studies and comparison of polarisation curves (e) before and after chronoamperometry and (f) 1000 CV cycles of the 10% FeP@B,N-V_2C heterostructure.

of 10% FeP@B,N-V_2C is only 118 mV dec^{-1}, which is lower than those of 5% (123 mV dec^{-1}), 15% (128 mV dec^{-1}), and 20% (130 mV dec^{-1}) FeP@B,N-V_2C heterostructures. In comparison, the Tafel slopes for Pt/C, FeP, and B,N-V_2C are 68 mV dec^{-1}, 127 mV dec^{-1}, and 124 mV dec^{-1}, respectively. These remarkable findings suggest that though we could not exceed the benchmark catalyst Pt/C, the overpotential and Tafel values are superior to those of the electrocatalysts mentioned in the previous literature (refer to Table S3 in the ESI†). The results indicate that the synergistic effect observed at the interface between FeP and dual-doped V_2C drives the performance of the prepared electrocatalysts to higher levels, thereby enhancing the transfer of charge carriers and mass transfer reaction, ultimately achieving maximum water reduction. The EIS measurements, as shown in Fig. 8c, clearly indicate lower resistance and higher flow of charge carriers for 10% FeP@B,N-V_2C compared to other materials, further confirming its superior electrocatalytic behavior (refer to Table S2 in the ESI†).

As in the study of the OER, we have also conducted stability and durability measurements for the HER using chronoamperometry and 1000 CV cycles. The 10% FeP@B,N-V_2C (Fig. 8d–f) catalyst maintained a stable current density over 24 hours with no significant change in overpotential, demonstrating the catalyst's durability. Similar stability was observed for other heterostructure electrocatalysts within the same time frame (Fig. S7†). Additionally, there was no appreciable change in the overpotential after 1000 CV cycles for the 10% FeP@B,N-V_2C heterostructure and other electrocatalysts, indicating minimal resistance to charge flow between the electrocatalyst and the electrode. Cyclic voltammetry at a sweep rate of 20–120 mV s^{-1} and within the potential window of 0.62–0.72 V *vs.* RHE (Fig. 7c and d for 10% FeP@B,N-V_2C and other catalysts in Fig. S9†) can be used to measure the C_{dl} values of the electrocatalyst. Notably, the ECSA values are higher for the 10% FeP@B,N-V_2C catalyst (3.71 mF cm^{-2}) than other catalysts (Table S2 in the ESI†). The quantification of H_2 produced at j_{10} (Fig. S12b†) revealed a high efficiency of 87% for 10% FeP@B,N-V_2C and the presence of hydrogen evolved was confirmed through GC-TCD analysis as illustrated in Fig. S13b.†

3.5. Plausible mechanism of the OER & HER

The OER mechanism involves four cooperative proton–electron transfer processes occurring at the active sites of catalysts. The first step is the hydroxide layer reaction (eqn (i)), in which the adsorption of OH^- ions on the electrode surface occurs through the loss of one electron. This reaction is followed by the oxide layer reaction (eqn (ii)), where the hydroxide layer further reacts with OH^- ions to form a metal oxide layer through the loss of one electron. The next step is the hydroxylation reaction (eqn (iii)), in which the OH^- ions react with the metal oxide layer, resulting in the formation of an oxyhydroxide layer by removing one electron. The final step is the O_2 adsorption reaction (eqn (iv)), where the oxyhydroxide layer reacts with OH^- ions to produce O_2.

$$M + OH^- \rightarrow MOH + e^- \quad (i)$$

$$MOH + OH^- \rightarrow MO + H_2O + e^- \quad (ii)$$

$$MO + OH^- \rightarrow MOOH + e^- \quad (iii)$$

$$MOOH + OH^- \rightarrow M + O_2 + H_2O + e^- \quad (iv)$$

In the OER mechanism outlined above, the hydroxylation reaction and the formation of M–OOH species are identified as the rate-limiting and rate-determining steps, respectively. The mechanism and reaction kinetics of the HER for the FeP@B,N-V_2C heterostructures were evaluated using calculated Tafel slope values. To theoretically assess the rate kinetics of the HER mechanism in an alkaline medium, reference Tafel slope values were obtained from the Volmer equation (eqn (v)) at 120 mV dec^{-1}, the Heyrovsky equation (eqn (vi)) at 40 mV dec^{-1}, and the Tafel equation (eqn (vii)) at 30 mV dec^{-1}.

$$H_2O + e^- \rightarrow H_{(ads)} + OH^- \quad (v)$$

$$H_{(ads)} + H_2O + e^- \rightarrow H_2 + OH^- \quad (vi)$$

$$H_{(ads)} + H_{(ads)} \rightarrow H_2 \quad (vii)$$

In these reactions, $H_{(ads)}$ indicates the presence of the hydrogen atom on the active site of the electrocatalyst. The initial Volmer reaction represents the discharge step, which generates $H_{(ads)}$ and necessitates a potential of 120 mV dec^{-1}. The subsequent step involves electrochemical desorption, which requires a potential of 40 mV dec^{-1} for the Heyrovsky reaction and 30 mV dec^{-1} for the Tafel reaction. In the current study, all electrodes exhibited Tafel slope values near 120 mV dec^{-1} (Table S1†), suggesting that each electrode adheres to the Volmer-Heyrovsky mechanism for the HER.[72–74]

3.6. Electrochemical overall water splitting (OWS)

Optimal performance in electrolysis requires distinct conditions when employing two different catalysts for the HER and the OER. Furthermore, the challenging conditions associated with water electrolysis—such as extreme pH levels, high potential, and the need for long-term stability—make the leaching and reconstruction of electrocatalysts inevitable. This phenomenon can result in significant cross-contamination between the electrodes if they utilize dissimilar materials. In contrast, bifunctional electrodes that use the same catalyst material for both the HER and OER present several advantages, including simplified production, broader applicability, and the prevention of cross-contamination.[75,76]

The 10% FeP@B,N-V_2C heterostructure demonstrated excellent bifunctional electrocatalytic water splitting (HER/OER) results. Therefore, it is interesting to test its ability as both an anode and cathode in a two-electrode configuration for overall water splitting (OWS). The performance was evaluated through LSV and chronoamperometry measurements in an H-type cell using an exchange membrane as a separator and 1 M KOH as the electrolyte. Fig. 9a illustrates the LSV graphs at a scan rate of 5 mV s^{-1}, showing a low cell voltage of 1.57 V@j_{10} for the 10% FeP@B,N-V_2C heterostructure, compared to 1.9 V, 1.79 V, and 1.91 V for 5%, 15%, and 20% FeP@B,N-V_2C heterostructures, respectively. We have observed an oxidation peak in between 1.4 V and 1.75 V in CV measurements and the same was reflected in the LSV plot. This may be due to ion oxidation in the electrolyte during water splitting.

As depicted in Fig. 9, long-term chronoamperometry and chronopotentiometry stability measurements indicate consistent performance with unchanged activity at 10 mA cm^{-2} current density for the 10% FeP@B,N-V_2C heterostructure

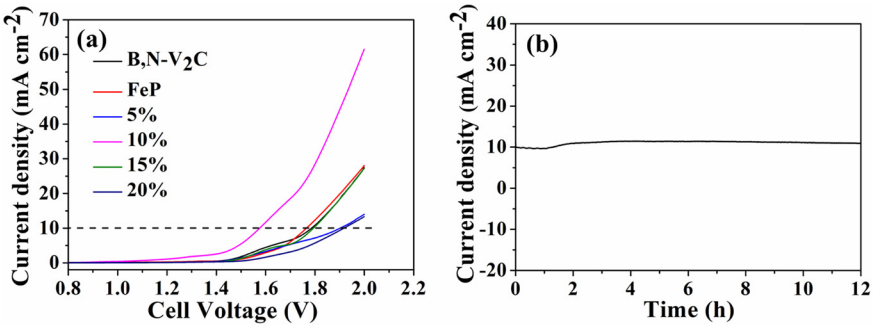

Fig. 9 (a) Polarization curves. (b) Chronoamperometry plot at an applied voltage of 1.57 V@j_{10} mA cm^{-2} for the 10% FeP@B,N-V_2C||10% FeP@B,N-V_2C as the anode and cathode for overall water splitting in 1 M KOH.

and other electrocatalysts (Fig. S10†). Some minor fluctuations in device stability may be attributed to excess bubble formation at the exposed electrode sites. An analysis of the 10% FeP@B,N-V_2C heterostructure after water electrolysis is presented in Fig. S11.† Comparative analysis with the previous literature (Table S4 in ESI†) demonstrates the superior electrocatalytic activity of the materials used in this study. The results validate the enhanced electrochemical stability and performance resulting from the heterojunction formed between the flakes and particle aggregation at the nanoscale.

The results from the RDE and H-cell experiments are essential, as they can be applied to full-cell experiments, offering valuable insights into the kinetics and reaction mechanisms of the anode and cathode materials. This transferability enables a more informed approach to the design and optimization of the full-cell, particularly in the selection of suitable materials, refinement of electrolyte composition, and comprehension of potential limitations related to mass transport and crossover effects.[77–82]

4. Conclusion

In this study, a non-noble metal-based catalyst comprising hierarchical boron and nitrogen co-doped V_2C nanoparticles on FeP nanoflakes as a substrate was successfully synthesized using a straightforward hydrothermal approach and pyrolysis method. Various advanced spectroscopic and microscopic techniques confirmed the structural and morphological features of the materials. The electrocatalysts exhibited highly efficient bifunctional electrochemical water splitting activity towards the HER/OER in an alkaline medium. Notably, the 10% FeP@B,N-V_2C heterostructure displayed superior electroactivity with remarkably low overpotential and Tafel values for the OER and HER, along with exceptional long-term stability and durability. The superior electrocatalytic behavior of the developed heterostructures is attributed to heterojunction formation between the nanoflakes and particles, resulting in efficient charge transfer and improved reaction kinetics. This study unequivocally demonstrates the successful formation of a heterointerface between FeP nanoflakes and V_2C nanoparticles and good improvement in electroactive centres due to the co-doping of B and N. These results not only contribute to the advancement of electrocatalysis, but also pave the way for the development of novel bifunctional self-supported electrocatalysts for enhanced energy generation.

Data availability

All data pertaining to this manuscript are available in the ESI.† We did not use any external data for our research.

Author contributions

Dasari Sai Hemanth Kumar, Manzoor Ahmad Pandit, Vinay Kumar Kolakaluri – data curation, formal analysis, investigation, methodology, and writing – original draft. Krishnamurthi Muralidharan – conceptualization, supervision, funding acquisition, and writing – review & editing.

Conflicts of interest

The authors declare no conflicts of interest.

Acknowledgements

The authors thank the Institute of Eminence (IoE) grant from the Ministry of Education, Government of India to University of Hyderabad (No UoH-IoE-RC3-21-043) for project and fellowship (DSHK). The instrument support grant from the Department of Science and Technology, New Delhi, India (through FIST program) is gratefully acknowledged.

References

1 S. H. K. Dasari, M. A. Pandit and K. Muralidharan, *Energy Fuels*, 2024, **38**, 17878–17890.
2 M. A. Pandit, S. H. K. Dasari, M. Ramadoss, Y. Chen and K. Muralidharan, *RSC Adv.*, 2022, **12**, 7762–7772.
3 M. Ramadoss, Y. Chen, X. Chen, Z. Su, M. Karpuraranjith, D. Yang, M. A. Pandit and K. Muralidharan, *J. Phys. Chem. C*, 2021, **125**, 20972–20979.
4 M. Ramadoss, M. A. Pandit, Y. Chen, M. Karpuraranjith and K. Muralidharan, *ACS Symp. Ser.*, 2022, **1431**, 227–255.
5 B. Li, J. Zhao, Y. Wu, G. Zhang, H. Wu, F. Lyu, J. He, J. Fan, J. Lu and Y. Y. Li, *Small*, 2023, **19**, 2301715.
6 M. R. Kandel, U. N. Pan, P. P. Dhakal, R. B. Ghising, T. T. Nguyen, J. Zhao, N. H. Kim and J. H. Lee, *Appl. Catal., B*, 2023, **331**, 122680.
7 S. Marimuthu, A. Shankar and G. Maduraiveeran, *Chem. Commun.*, 2023, **59**, 2600.
8 C. Chen, Y. Kang, Z. Huo, Z. Zhu, W. Huang, H. L. Xin, J. D. Snyder, D. Li, J. A. Herron, M. Mavrikakis, M. Chi, K. L. More, Y. Li, N. M. Markovic, G. A. Somorjai, P. Yang and V. R. Stamenkovic, *Science*, 2014, **343**, 1339–1343.
9 J. Pei, J. Mao, X. Liang, C. Chen, Q. Peng, D. Wang and Y. Li, *Chem. Commun.*, 2016, **52**, 3793–3796.
10 H. Pei, L. Zhang, G. Zhi, D. Kong, Y. Wang, S. Huang, J. Zang, T. Xu, H. Wang and X. Li, *Chem. Eng. J.*, 2022, **433**, 133643.
11 S. Anantharaj, S. R. Ede, K. Sakthikumar, K. Karthick, S. Mishra and S. Kundu, *ACS Catal.*, 2016, **6**, 8069–8097.
12 M. R. Kandel, U. N. Pan, D. R. Paudel, P. P. Dhakal, N. H. Kim and J. H. Lee, *Composites, Part B*, 2022, **239**, 109992.
13 Y. G. Zhao, N. Dongfang, C. A. Triana, C. Huang, R. Erni, W. C. Wan, J. G. Li, D. Stoian, L. Pan, P. Zhang, J. G. Lan, M. Iannuzzi and G. R. Patzke, *Energy Environ. Sci.*, 2022, **15**, 727–739.
14 Y.-N. Wang, Z.-J. Yang, D.-H. Yang, L. Zhao, X.-R. Shi, G. Yang and B.-H. Han, *ACS Appl. Mater. Interfaces*, 2021, **13**, 8832–8843.
15 Y. Shi and B. Zhang, *Chem. Soc. Rev.*, 2016, **45**, 1529–1541.

16 J. Y. Wang, W. Li, X. F. Chen and A. S. Huang, *J. Alloys Compd.*, 2023, **934**, 167828.
17 Z. S. Zhao, W. Jin, L. Xu, C. Wang, Y. Zhang and Z. X. Wu, *J. Mater. Chem. A*, 2021, **9**, 12074–12079.
18 M. B. Zhang, X. Ma, H. Zhong, J. Yang and Z. F. Cao, *J. Alloys Compd.*, 2023, **935**, 168135.
19 Y. X. Liu, Z. M. Tian, Q. C. Xu, Y. X. Yang, Y. T. Zheng, H. G. Pan, J. Chen, Z. Wang and W. J. Zheng, *ACS Appl. Mater. Interfaces*, 2022, **14**, 8963–8973.
20 A. Abdollahi, A. Ghaffarinejad and M. Arabi, *J. Alloys Compd.*, 2023, **937**, 168400.
21 A. Zou, A. Du and X. Yao, *Adv. Mater.*, 2017, **29**, 1700017.
22 K. P. Singh, E. J. Bae and J. S. Yu, *J. Am. Chem. Soc.*, 2015, **137**, 3165–3168.
23 M. Li, T. Liu, X. Bo, M. Zhou, L. Guo and S. Guo, *Nano Energy*, 2017, **33**, 221–228.
24 L. Feng, Y. Liu and J. Zhao, *Phys. Chem. Chem. Phys.*, 2015, **17**, 30687–30694.
25 P. Jiang, Q. Liu, Y. Liang, J. Tian, A. M. Asiri and X. Sun, *Angew. Chem., Int. Ed.*, 2014, **53**, 12855–12859.
26 D. Li, H. Baydoun, B. Kulikowski and S. L. Brock, *Chem. Mater.*, 2017, **29**, 3048–3054.
27 Y. Luo, M. Gong, J. Wang, P. Zhao, X. Yang, S. Cui, Z. Li, Z. Jiao and L. Cheng, *Colloids Surf., A*, 2022, **655**, 130119.
28 X. Y. Li, F. Y. Duan, X. Y. Lu, Y. F. Gang, W. L. Zheng, Y. Y. Lin, L. Z. Chen, Y. Y. Dan and X. F. Cheng, *J. Alloys Compd.*, 2023, **935**, 168128.
29 J. Wu, W. Chen, H. Zheng, M. Chen, J. Xia and X. Qian, *J. Alloys Compd.*, 2023, **945**, 169357.
30 Z. Xu, M. Hao, X. Liu, J. Ma, L. Wang, C. Li and W. Wang, *Catalysts*, 2022, **12**, 1417.
31 Y. Zhang, H. Guo, X. Li, W. Ren and R. Song, *Mater. Chem. Front.*, 2022, **6**, 1477–1486.
32 Z. Li, Z. Li, H. Yao, Y. Wei and J. Hu, *J. Colloid Interface Sci.*, 2024, **653**, 857–866.
33 Z.-Y. Yu, Y. Duan, M.-R. Gao, C.-C. Lang, Y.-R. Zheng and S.-H. Yu, *Chem. Sci.*, 2017, **8**, 968–973.
34 N. Wang, X. Bo and M. Zhou, *ACS Appl. Mater. Interfaces*, 2022, **14**, 23332–23341.
35 L. Cao, N. Zhang, L. Feng, D. He, K. Kajiyoshi, X. Li, Q. Huang, L. Feng, J. Huang and R. Li, *Inorg. Chem. Front.*, 2020, **7**, 4142–4149.
36 J. Wan, C. Wang, Q. Tang, X. Gu and M. He, *RSC Adv.*, 2019, **9**, 37467–37473.
37 C. Yang, R. Zhao, H. Xiang, J. Wu, W. Zhong, W. Li, Q. Zhang, N. Yang and X. Li, *Adv. Energy Mater.*, 2020, **10**, 2002260.
38 L. Peng, J. Shen, L. Zhang, Y. Wang, R. Xiang, J. Li, L. Li and Z. Wei, *J. Mater. Chem. A*, 2017, **5**, 23028–23034.
39 R. Zhao, C. Yang, Q. Zhang, H. Xiang, Y. Li and X. Li, *J. Phys. Chem. C*, 2021, **125**, 14607–14615.
40 M. Shao, H. Chen, S. Hao, H. Liu, Y. Cao, Y. Zhao, J. Jin, H. Dang, Y. Meng, Y. Huo and L. Cui, *Appl. Surf. Sci.*, 2022, **577**, 151857.
41 M. Yang, Y. Yang, K. Wang, S. Li, F. Feng, K. Lan, P. Jiang, X. Huang, H. Yang and R. Li, *Electrochim. Acta*, 2020, **337**, 135685.
42 F. Guo, Z. Liu, J. Xiao, X. Zeng, C. Zhang, Y. Lin, P. Dong, T. Liu, Y. Zhang and M. Li, *Chem. Eng. J.*, 2022, **446**, 137111.
43 T. Liu, M. Li, X. Bo and M. Zhou, *J. Colloid Interface Sci.*, 2019, **533**, 709–722.
44 Y. Kang, W. Wang, J. Li, S. Imhanria, Y. Hao and Z. Lei, *J. Power Sources*, 2021, **493**, 229665.
45 P. Joshi, R. Yadav, M. Hara, T. Inoue, Y. Motoyama and M. Yoshimura, *J. Mater. Chem. A*, 2021, **9**, 9066–9080.
46 Z. Lin, Z. Huan, J. Zhang, J. Li, Z. Li, P. Guo, Y. Zhu and T. Zhang, *Chemosphere*, 2022, **292**, 133373.
47 J. Godwin, N. Abdus-Salam, A. I. Haleemat, P. K. Panda, J. Panda and B. C. Tripathy, *Inorg. Chem. Commun.*, 2022, **140**, 109346.
48 (*a*) A. S. Ahmed, T. Ahamad, N. Ahmad and M. Z. Khan, *Mater. Chem. Phys.*, 2019, **238**, 121906; (*b*) M. Sandhya, D. Ramasamy, K. Sudhakar, K. Kadirgama and W. S. W. Harun, *Ultrason. Sonochem.*, 2021, **73**, 105479.
49 (*a*) R. Monsef, F. Soofivand, H. A. Alshamsi, A. Al-Nayili, M. Ghiyasiyan-Arani and M. Salavati-Niasari, *J. Mol. Liq.*, 2021, **336**, 116339; (*b*) S. Sekar, C. Bathula, I. Rabani, J. W. Lee, S. H. Lee, Y.-S. Seo and S. Lee, *Ultrason. Sonochem.*, 2022, **90**, 106177.
50 M. Junaid, M. H. M. Khir, G. Witjaksono, N. Tansu, M. S. M. Saheed, P. Kumar, Z. Ullah, A. Yar and F. Usman, *Molecules*, 2020, **25**, 3646.
51 H. K. Sadhanala and K. K. Nanda, *J. Phys. Chem. C*, 2015, **119**, 13138–13143.
52 X. Xu, C. Shi, R. Chen and T. Chen, *RSC Adv.*, 2017, **7**, 22263–22269.
53 C. Liu, H. Pan, H. Hu, W. Wei, Q. Lu, C. Zhao, H. Wang and F. Du, *Amino Acids*, 2022, **54**, 1173–1181.
54 J. Xia, H. Guo, G. Yu, Q. Chen, Y. Liu, Q. Liu, Y. Luo, T. Li and E. Traversa, *Catal. Lett.*, 2021, **151**, 3516–3522.
55 Z. Ahsan, Z. Cai, S. Wang, Y. Ma, G. Song, M. Yu, S. Zhang, W. Yang, C. Wen and X. Feng, *J. Solid State Electrochem.*, 2021, **25**, 2127–2137.
56 H. K. Sadhanala and K. K. Nanda, *Carbon*, 2016, **96**, 166–173.
57 Y. Yang, *et al.*, *ACS Appl. Mater. Interfaces*, 2015, **7**, 27324–27330.
58 X. Y. Hu, M. Huang, X. Meng and X. Ju, *RSC Adv.*, 2019, **9**, 42110–42119.
59 L. Gao, T. Ma, L. Zhang and X. Yang, *J. Solid State Electrochem.*, 2021, **25**, 2055–2063.
60 Y. Feng, C. Xu and E. Hu, *et al.*, *J. Mater. Chem. A*, 2018, **6**, 14103.
61 Y. Liu, B. Wang and Y. Lu, *et al.*, *J. Mater. Sci.*, 2021, **56**, 16000–16009.
62 Y. Yao, N. Mahmood and L. Pan, *et al.*, *Nanoscale*, 2018, **10**, 21327.
63 B. Peng, Y. Xu, K. Liu, X. Wang and F. M. Mulder, *ChemElectroChem*, 2017, **4**, 2140.
64 R. J. Liu, L. X. Yang and Y. Wang, *et al.*, *J. Solid State Electrochem.*, 2022, **26**, 831–842.
65 C. E. Iheomamere, C. L. Arnold and J. Summers, *et al.*, *J. Mater. Sci.: Mater. Electron.*, 2022, **33**, 974–984.

66 J. Qu, Q. Li, C. Luo, J. Cheng and X. Hou, *Coatings*, 2018, **8**, 214.
67 R. R. Solís, M. A. Quintana, G. Blázquez, M. Calero and M. J. Muñoz-Batista, *Catal. Today*, 2023, **423**, 114266.
68 W. Wang, B. Jiang and W. Xiong, *et al.*, *Sci. Rep.*, 2013, **3**, 3383.
69 M. A. Pandit, S. H. K. Dasari, S. Billakanti, M. Ramadoss and K. Muralidharan, *J. Phys. Chem. C*, 2020, **124**, 18010–18019.
70 M. Zhou, H. L. Wang and S. Guo, *Chem. Soc. Rev.*, 2016, **45**, 1273–1307.
71 Irkham and E. Yasuaki, *Analyst*, 2019, **144**, 4499–4504.
72 N. T. Suen, S. F. Hung, Q. Quan, N. Zhang, Y. J. Xu and H. M. Chen, *Chem. Soc. Rev.*, 2017, **46**, 337–365.
73 G. P. Kamble, A. A. Kashale, A. S. Rasal, S. A. Mane, R. A. Chavan, J. Y. Chang, Y. C. Ling, S. S. Kolekar and A. V. Ghule, *RSC Adv.*, 2021, **11**, 3666–3672.
74 M. M. Rajpure, H. A. Bandal, H. S. Jadhav and H. Kim, *J. Electroanal. Chem.*, 2022, **923**, 116825.
75 P. W. Menezes, A. Indra, I. Zaharieva, C. Walter, S. Loos, S. Hoffmann, R. Schlogl, H. Dau and M. Driess, *Energy Environ. Sci.*, 2019, **12**, 988.
76 L. Quan, H. Jiang, G. Mei, Y. Sun and B. You, *Chem. Rev.*, 2024, **124**(7), 3694–3812.
77 M. Li, S. A. Odom and A. R. Pancoast, *et al.*, *ACS Energy Lett.*, 2021, **6**(11), 3932–3943.
78 J. M. E. Bastian, K. Ulrike, T. Simon, D. Andreas, K. Elias and T. Thomas, *Chem. Eng. J.*, 2021, **424**, 130501.
79 A. H. M. da Silva, R. E. Vos, R. J. C. Schrama and M. T. M. Koper, *Electrochim. Acta*, 2024, **498**, 144612.
80 L. Fan, Z. Tu and S. H. Chan, *Energy Rep.*, 2021, **7**, 8421–8446.
81 Z. Luthey-Schulten, *Nat. Methods*, 2021, **18**, 446–447.
82 A. Landman, R. Halabi, P. Dias and H. Dotan, *et al.*, *Joule*, 2020, **4**, 448–471.